Dalton Transactions

ROYAL SOCIETY OF CHEMISTRY

PAPER

View Article Online
View Journal | View Issue

Cite this: *Dalton Trans.*, 2026, **55**, 5197

Pendant-cation assisted spontaneous axial halide substitution in group 7 M(L)(CO)$_3$X complexes

Wesley W. Kramer, *[a,b] Thomas R. Sheridan, †[b] Jorge Pérez-Vázquez, ‡[a] Christophe A. Boivin, §[a] Amanda M. Browne, [a] Catherine G. Logan [a] and Brian C. Sanders ¶[b]

The installation of cationic pendant groups proximal to catalyst active sites has resulted in improved performance for electrocatalytic CO_2 reduction (CO2R) by molecular catalysts. It is not well understood how pendant cationic groups, designed to stabilize anionic CO_2 reduction intermediates, interact with the axial halide ligands of M(diimine)(CO)$_3$X (M = Re, Mn; X = Cl, Br), an important class of molecular CO2R electrocatalysts. We observe that in [M(tmam)(CO)$_3$X]$^{2+}$ complexes (**1**: M = Re, X = Cl; **2**: M = Mn, X = Br, tmam^{2+} = 4,4′-methylenetrimethylammonium-2,2′-bipyridine) bearing the dicationic tmam^{2+} ligand, the cationic pendant groups facilitate the spontaneous exchange of the axial halide for solvent molecules (MeCN or H_2O), a highly unusual behavior for this class of complexes. We present a study of the thermodynamics and kinetics of these reactions under aqueous and non-aqueous conditions. The extent to which this reaction occurs was found to depend on the identity of the metal, with substitution being more favorable for Mn than Re, and the solvent and halide substitution was more favorable in H_2O than MeCN for both complexes. ^{1}H NMR kinetics experiments for axial chloride substitution for **1** in D_2O suggest a second-order dependence on complex concentration, indicating an intermolecular process. The halide-substitution reaction had little effect on the electrochemistry of the complexes in cyclic voltammetry experiments due to the reductive instability (deamination) of tmam^{2+}. This study demonstrates that cationic pendant groups are *noninnocent*, actively modulating the coordination environment of the catalyst, which provides key insights into their potential roles in catalyst activation.

Received 9th October 2025,
Accepted 6th January 2026

DOI: 10.1039/d5dt02433a

rsc.li/dalton

Introduction

Carbon dioxide reduction (CO2R) is a critical reaction for the creation of carbon-neutral fossil fuels. However, due to the inert structure of carbon dioxide, large overpotentials are generally required for catalysis, making CO_2 reduction at scale economically challenging. As one of the prototypical CO_2 reduction (CO2R) electrocatalyst, group 7 M(bpy)(CO)$_3$X (bpy = 2,2′-bipyridine)[1–3] complexes have been useful models to test concepts in catalyst design, owing to their well-defined catalytically active sites and the readily modifiable bipyridine ligand scaffold. Ligand modification strategies have provided insights into how to influence and improve electrocatalytic CO_2 reduction *via* modifications of the ligand electronic structure through the introduction of electron-donating or -withdrawing groups,[4–6] introducing steric hindrance near the catalytic center,[7] and groups that modify the secondary coordination sphere.[8–11] One promising approach has shown that ligands modified with positively charged groups can reduce the overpotential required for CO_2R through secondary-sphere electrostatic interactions that stabilize the negatively charged CO_2 reduction intermediate.[12–17] This electrostatic effect has been shown to significantly improve catalytic activity and lower overpotentials for CO_2 reduction in both iron tetraphenylporphyrin[12] and Re(bpy-R)(CO)$_3$Cl[13–17] derivatives using ligands modified with cationic pendant groups positioned near the metal center. Recent work by Thoi and coworkers sought to study the effects of the cationic groups of the tmam^{2+} (tmam^{2+} = 4,4′-methylenetrimethylammonium-2,2′-bipyridine) ligand on the electrocatalytic CO2R performance of rhenium tricarbonyl catalysts.[18] This work found that the trimethyl ammonium functional groups are prone to reductive deamination of the pendant groups at potentials significantly positive of the onset of CO2R catalysis, making the study of their

[a]*Department of Chemistry, Hamilton College, Clinton, NY 13323, USA. E-mail: wkramer@hamilton.edu*
[b]*Division of Chemistry and Chemical Engineering, California Institute of Technology, Pasadena, CA 91125, USA*
†Current institution: Sandia National Laboratory, Albuquerque, NM 87123, USA.
‡Current institution: Department of Chemistry, University of Michigan, Ann Arbor, MI 48109, USA.
§Current Institution: Department of Chemistry, University of Rochester, Rochester, NY 14627, USA.
¶Current institution: Biosciences Division, Oak Ridge National Laboratory, Oak Ridge, TN 37830, USA.

effect on CO2R impossible. Nonetheless, this work highlights both the promise and challenges of incorporating charged functional groups into ligand frameworks. In particular, the $tmam^{2+}$ scaffold provides a valuable model for understanding how charged pendants can tune the electronic structure, coordination environment, and ultimately the catalytic behavior of transition metal complexes.

An understudied aspect of cationic pendant groups in the secondary coordination sphere is how these groups affect the ligands in the primary coordination sphere. In the parent complex, $Re(bpy)(CO)_3Cl$, the first 1-e$^-$ reduction is localized on the bipyridine ligand, resulting in the formation of $[Re^{I}(bpy^{\bullet-})(CO)_3Cl]^-$, while the second 1-e$^-$ reduction is Re-centered and results in $[Re^{0}(bpy^{\bullet-})(CO)_3]^-$. The dissociation of the axial Cl^- is necessary to open a coordination site for CO_2 binding. Several groups have shown that the use of bipyridine ligands functionalized with cationic groups can promote the dissociation of halide following the first reduction by stabilizing the release of the anion and lowering the onset potential of CO2R.[13–17] The binding affinity between halide ions and the cationic ligand binding pockets has been shown to aid the dissociation of the axial halide of the group 7 tricarbonyl catalysts upon reduction.[16] Anion binding with the $tmam^{2+}$ ligand has been studied in some detail for a series of $[Ru(tmam)_n(bpy)_{3-n}]^{(2+2n)+}$ complexes.[19–25] This work demonstrated that halides have a greater binding affinity with the cationic binding pockets of the $tmam^{2+}$ ligands than the larger PF_6^- anions used to solubilize the complexes in non-aqueous solvents. The ligand's greater affinity for binding halides in its binding pocket, and proximity to the active site of the $[M(tmam)(CO)_3X]^{2+}$ complex may interact with the axial halide. However, the extent to which cationic groups of these complexes interact with the axial halide in their unreduced state has not been investigated.

To this end, we have synthesized a series of Re and Mn tricarbonyl complexes with the $tmam^{2+}$ ligand $[M(tmam)(CO)_3X](Y)_2$ (M = Mn, Re; X = Br, Cl; Y = PF_6^-, Cl^-) to study their behavior in H_2O and MeCN. Through ^1H NMR, IR, and UV-vis spectroscopy, we have measured the effect of proximal positively charged groups on the lability of the axial halide. Interestingly, halide substitution by the solvent is observed for all complexes. We find that the extent of substitution depends on both the identity of the metal (with Mn being far more favorable to substitution than Re) and the solvent. The thermodynamics of this halide exchange process has been quantified using ^1H NMR studies. Based on ^1H NMR kinetics, a second order mechanism for halide dissociation involving two $M(tmam)^{2+}$ complexes is proposed. Additionally, electrochemical studies in both aqueous and non-aqueous solvents were used to understand the influence of halide substitution chemistry on the electrochemical response of the complexes.

Results and discussion

Synthesis and characterization

Dicationic $[M(tmam)(CO)_3X](PF_6)_2$ complexes were prepared by refluxing a solution of $[tmam](PF_6)_2$ and the appropriate

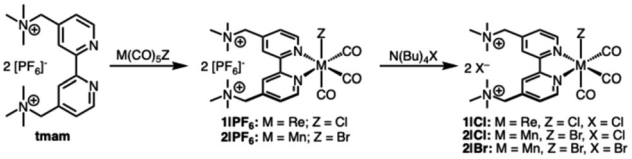

Scheme 1 Synthesis of cationic $[Re(tmam)(CO)_3Cl]X_2$ (**1|X**) and $[Mn(tmam)(CO)_3Br]X_2$ (**2|X**) complexes.

$M(CO)_5X$ (M = Re, X = Cl; M = Mn, X = Br) in acetone as shown in Scheme 1. Acetone was chosen as the solvent for this reaction to promote the solubility of the $tmam^{2+}$ ligand. The products, $[Re(tmam)(CO)_3Cl](PF_6)_2$ (**1|PF$_6$**) and $[Mn(tmam)(CO)_3Br](PF_6)_2$ (**2|PF$_6$**), were precipitated from the reaction mixture by the addition of Et_2O. The H_2O-soluble salts, $[Re(tmam)(CO)_3Cl](Cl)_2$ (**1|Cl**) and $[Mn(tmam)(CO)_3Br](Cl)_2$ (**2|Cl**), were precipitated from the acetone reaction mixture by the addition of excess TBACl. The various salts of these metal complexes were obtained in 76–92% yields. $[Mn(tmam)(CO)_3Br](Br)_2$ (**2|Br**) was prepared by treating a concentrated acetone solution of **2|PF$_6$** with excess TBABr to afford 41% yield. The lower yield of **2|Br** stems from its increased solubility in acetone, leading to loss of product during purification. The identity and purity of all complexes were confirmed using ^1H and ^{13}C NMR, FTIR, mass spectrometry, and elemental analysis. ^1H NMR and FTIR data for **1|PF$_6$** agree with previously published spectroscopic data for $[Re(tmam)(CO)_3Br][PF_6]_2$.[18] The MeCN adducts of **1** and **2** were prepared by treating MeCN solutions of complexes **1|PF$_6$** and **2|PF$_6$**, respectively, with $AgPF_6$.

X-ray quality crystals of **1** and **2** were grown by slow diffusion of Et_2O into MeCN. Interestingly, crystals of the tricationic MeCN adduct $[Re(tmam)(CO)_3(MeCN)](PF_6)_3$ (**1-MeCN$^+$**) were grown by slow diffusion of Et_2O into a MeCN solution containing **1|PF$_6$** and excess NH_4PF_6. Typically, Ag salts are required to remove the chloride from these Re complexes.[26] X-ray quality crystals of **1|Cl**, **2|Cl**, and **2|Br** could not be grown. X-ray crystal structures of **2|PF$_6$** are shown in Fig. 1, and those of **1|PF$_6$** and **1-MeCN$^+$** are shown in Fig. S1 and S2. The solid-state structures of **1|PF$_6$** and **2|PF$_6$** show the pendant trimethylammonium groups oriented opposite the bipyridine plane from the axial halide. M–X bond distances (**1|PF$_6$**: Re–Cl

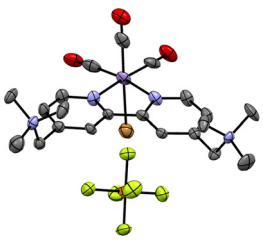

Fig. 1 ORTEP structures (50% thermal probability for all non-hydrogen atoms) of $[Mn(TMAM)(CO)_3(Br)](PF_6)_2$ (**2|PF$_6$**) showing PF_6^- in the cationic pocket.

= 2.487 Å, **2|PF$_6$**: Mn–Br = 2.534 Å) agree with those of comparable Re and Mn tricarbonyl complexes.[3,27,28] In all three structures, a PF_6^- anion is situated in the dicationic binding pocket of the tmam^{2+} ligand. This close pairing of the PF_6^- is typically observed in the crystal structures of tmam^{2+} complexes.[18,20,25]

Spectroscopic characterization

The ATR FT-IR spectra of **1|X** and **2|X** complexes are shown in Fig. S3 and S4 and the CO stretching frequencies are listed in Table 1. The solid-state FT-IR spectra of **1|PF$_6$** and **1|Cl** show three dominant CO stretches as expected for a *fac* tricarbonyl complex. However, the lower energy CO stretches are significantly broadened, and in the spectrum of **1|Cl**, both peaks display clear shoulders. The ATR spectra of the **2|X** complexes still show three major peaks, but the spectra are complicated by additional CO stretches around the low energy CO. The presence of these broadened spectra and additional CO peaks may indicate that the complexes have adopted multiple packing arrangements in the solid state.[29] The IR spectra of **1|PF$_6$**, **1-MeCN$^+$**, **2|PF$_6$**, and **2-MeCN$^+$** exhibit a P–F stretch at 823 cm^{-1}, and this signal is absent from the spectra of **1|Cl**, **2|Cl**, and **2|Br**, confirming complete salt metathesis. The solution phase FTIR spectra of **1|PF$_6$** and **2|PF$_6$** in MeCN (Fig. S5) are comparable to the solid-state spectra but are significantly sharper. The FTIR spectrum of **1|PF$_6$** shows three sharp peaks.

For **2|PF$_6$**, more complex behavior is observed in the solution phase. The FTIR spectrum of freshly prepared solutions shows three CO stretches at 2030, 1941, and 1929 cm^{-1}. However, over time, additional peaks emerge at 2051 and 1961 cm^{-1}. As shown in Fig. 2, these new peaks correspond to the presence of **2-MeCN$^+$** in solution. Addition of TBABr to the sample shifts the spectrum back towards the original, suggesting a ligand substitution equilibrium in which the axial Br$^-$ ligand is displaced by MeCN. This phenomenon is discussed in more detail below.

The UV-vis spectra of **1|X** and **2|X** were obtained in DMSO and are shown in Fig. 3. Peak maxima are given in Table 1. For both **1|X** and **2|X**, the identity of the counterion X$^-$ had only minor effects on the absorption spectrum of the complex. All

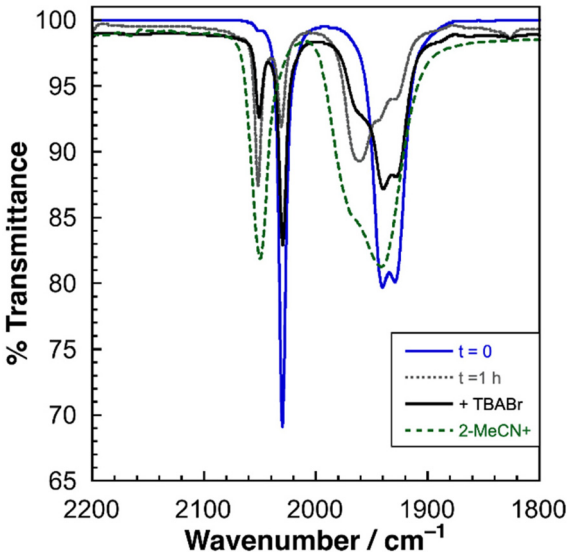

Fig. 2 Solution FTIR spectra showing a freshly prepared solution of **2|PF$_6$** in MeCN (blue), **2|PF$_6$** after 1 h in MeCN (grey), following the addition of excess TBABr to the *t* = 1 h solution of **2|PF$_6$** (black), and an ATR spectrum of **2-MeCN$^+$** (green).

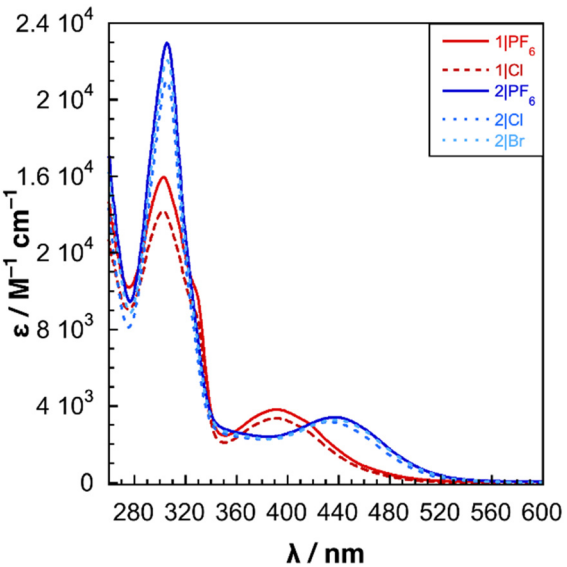

Fig. 3 UV-vis spectra of complexes **1|X** and **2|X** obtained in DMSO. Molar absorptivity of each complex was calculated from a linear fit derived from absorbance at 5 different concentrations.

Table 1 Collected FTIR and UV-vis data for complexes **1|X**, **1-MeCN$^+$**, **2|X**, and **2-MeCN$^+$**

Complex	ν_{CO} (cm^{-1})	λ/nm (ε/M^{-1} cm^{-1})
1|PF$_6$[a]	2018, 1919, 1891, (2025, 1923, 1904)[b]	302 (14 000), 390 (3800)
1|Cl[a]	2023, 1910, 1873	303 (16 000), 390 (3400)
1-MeCN$^+$[b]	2039, 1919br	249 (18 000), 284 (15 000), 312 (13 000), 326 (13 000), 359 (4300)
2|PF$_6$[a]	2023, 1944, 1931, 1911, (2030, 1941, 1929)[b]	305 (23 000), 437 (3400)
2|Cl[a]	2024, 1934, 1924, 1901	305 (21 000), 433 (3200)
2|Br[a]	2023, 1934(sh), 1907	305 (22 000), 437 (3300)
2-MeCN$^+$[b]	2049, 1941 br	246 (15 000), 296 (20 000), 389 (3700)

[a] Spectra collected in DMSO. [b] Spectra collected in MeCN.

salts of compound **1** display an MLCT absorption at 390 nm and a tmam^{2+} π–π* transition at 303 nm with a shoulder at 326 nm. For compound **2** salts, the MLCT band of **2|Cl** (433 nm) is blue-shifted by 4 nm compared to **2|PF$_6$** and **2|Br** which both appear at 437 nm. All three compounds exhibit a tmam^{2+} π–π* transition at 305 nm. Though the effect is small, the identity of the counterion primarily affects the molar absorptivity of the complexes. The near uniformity of the absorption spectra of the **1|X** and **2|X** salts suggests that ion

pairing with the $tmam^{2+}$ ligand has little effect on the electronic structure of the complexes. Minor changes in the absorption spectrum of $[Ru(tmam)_n(L)_m]^{(2+2n)+}$ complexes upon anion exchange have been observed.[20] The UV-vis spectra of **1-MeCN$^+$** and **2-MeCN$^+$** in MeCN are shown in Fig. S6 and peak data are summarized in Table 1. For **1-MeCN$^+$**, the MLCT peak appears at 359 nm, and the π–π* transitions are split into several distinct peaks. The UV-vis spectrum of **2-MeCN$^+$** also displays a blue-shifted MLCT absorption at 389 nm and a broadened π–π* transition centered at 296 nm with a shoulder at 324 nm (not observed in the spectrum of **2|PF$_6$**).

The ^{1}H NMR spectra of all **1|X** and **2|X** complexes in deuterated dimethylsulfoxide (DMSO-d_6) are shown in Fig. S7–S11 and chemical shifts are tabulated in Table 2. All complexes in DMSO-d_6 show a single species consistent with the crystal structures. For all complexes, the methylene protons of the $tmam^{2+}$ ligand appear in a roofed doublet pattern (Fig. S7–S11). This is consistent with the presence of an anion in the $tmam^{2+}$ binding pocket. This locks the pendant arms in place and renders the two methylene protons inequivalent.[20] While the identity of the anion did not have a significant impact on the UV-vis spectra of these complexes, the NMR spectra are more sensitive to electrostatic interactions between the anion and the binding pocket and are, therefore, more sensitive to changes in the counterion. For both **1** and **2**, substitution of PF_6^- for Cl^- results in a large downfield shift for the 3,3′ protons of the bipyridine. While the 5,5′ peak shifts slightly upfield, the 6,6′ protons are unaffected by anion exchange. Smaller downfield shifts were also observed for the protons of the pendant groups. Similar downfield shifts are observed for **2|Br** in comparison with **2|PF$_6$**, though the shifts are smaller than those observed for **2|Cl**. The extent of the downfield shift is correlated with the strength of the interaction between the anion and the electropositive 3,3′ protons.[20–22] The trend in the position of the 3,3′ peaks of the **2|X** complexes, Cl^- (9.27 ppm) > Br^- (9.11 ppm) > PF_6 (8.66 ppm), correlates with increasing anion sizes. This behavior is consistent with observations of $[Ru(tmam)(L)_2]^{4+}$ complexes titrated with TBAI or TBACl.[20–22]

Table 2 Tabulated ^{1}H NMR peak data for complexes obtained in DMSO-d$_6$

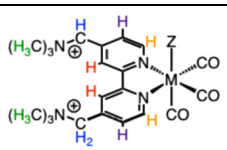

	5,5′	3,3′	6,6′	CH_2	$N(CH_3)_3$
1|PF6	9.22	8.75	7.94	4.74	3.18
1|Cl	9.18	9.51	7.94	4.84	3.23
2|PF6	9.4	8.66	7.90	4.73	3.18
2|Cl	9.34	9.27	7.90	4.82	3.22
2|Br	9.38	9.11	7.90	4.81	3.22

Halide substitution equilibria

Halide substitution in MeCN. Consistent with the solution-phase FTIR spectra of **2|PF$_6$** in MeCN solution, unusual halide substitution behaviour was observed in the ^{1}H NMR spectra of complexes **1|PF$_6$** and **2|PF$_6$** collected in MeCN-d_3. All samples were prepared at a concentration of 10 mM, and prior to sample preparation the complexes had not been previously exposed to MeCN. The ^{1}H NMR spectrum of **1|PF$_6$** in MeCN-d_3 taken immediately following sample preparation shows a small doublet at 7.85 ppm—downfield of the 6,6′ peak of **1|PF$_6$** (7.78 ppm)—that was not observed in the DMSO-d^6 spectrum of **1|PF6**. New 3,3′ and 5,5′ peaks are evident, but the new peaks significantly overlap with the original peak or their ^{13}C satellite peaks (Fig. 4). Over a period of hours, the secondary peaks became sharper. As the new doublet grew, a small downfield shift of the 3,3′ peak ($\Delta\delta$ = 0.03 ppm) was observed. The evolution of the ^{1}H NMR spectrum of **1|PF$_6$** in MeCN-d_3 is shown in Fig. S12. The appearance of a new species in solution and the downfield shift of the protons in the $tmam^{2+}$ binding pocket suggest the presence of free Cl^- formed by a substitution reaction with MeCN to form **1-MeCN$^+$** as shown in Scheme 2. Comparing the ^{1}H NMR spectra of the equilibrated sample of **1|PF$_6$** to the spectrum of **1-MeCN$^+$** (Fig. S13) shows that the chemical shifts of new species are identical to those of **1-MeCN$^+$**, supporting the proposed halide substitution reaction. The equilibrium constants for the halide substitution reactions were determined according to the general equilibrium expression $K_{eq} = \frac{(\mathbf{M}{-}Solv^+)(Z^-)}{(\mathbf{M})}$ using the average normalized peak areas for the aromatic protons of the parent complex (**M**), M = **1** or **2**, and the solvato species (**M-Solv$^+$**), Solv = MeCN or H_2O. The concentration of the liberated axial halide (Z^- = Cl^- or Br^-) is assumed to be $[Z^-] = [\mathbf{M\text{-}Solv}^+]$. K_{eq} = 7.94 ± 0.84 × 10^{-4} for the equilibrium between **1** and **1-MeCN$^+$**. Equilibrium constants and thermodynamic data for these halide substitution reactions are given in Table 3. This behavior is rare for $Re(L)(CO)_3X$ complexes.[30] Preparation of solvato complexes for this class of compounds generally requires the use of Ag salts. We hypothesize that the cationic pendant groups of the $tmam^{2+}$ ligand enable the halide substitution chemistry observed for **1** *via* their capacity to stabilize the release of the halide into the dicationic binding pocket. Qualitatively similar behavior was noted for a recently reported $[Re(L^{2+})(CO)_3Cl]^{2+}$ (L^{2+} = 6,6′-(2-((trimethylamonium)-methyl) phenyl)-2,2′-bipyridine) complex, which showed a slow evolution of its ^{1}H NMR spectrum that was attributed to interconversion between rotamers of the large pendant groups.[13] However, in light of our observations, it is possible that the authors were observing a slow chloride substitution reaction in MeCN-d_3.

Complex **2|PF$_6$** also displays halide substitution behavior in MeCN, but with a larger K_{eq} compared to **1|PF$_6$**. The initial ^{1}H NMR spectrum of **2|PF$_6$** in MeCN-d_3 showed significantly broadened peaks. Over the course of one hour, the peaks sharpened and peaks corresponding to a second Mn(tmam)

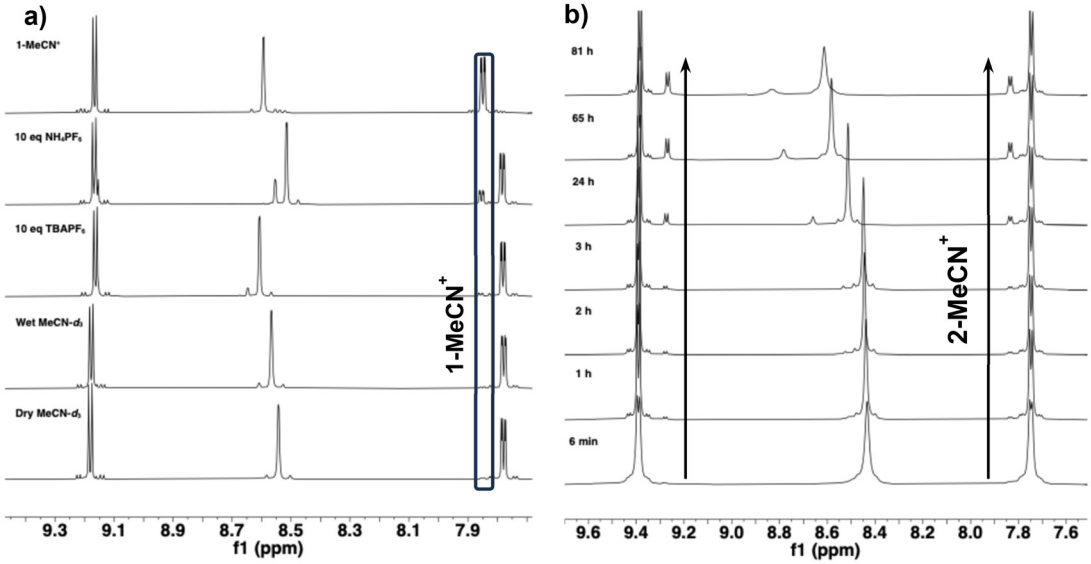

Fig. 4 ^{1}H NMR spectra in MeCN-d_3 of (a) **1|PF$_6$** under various conditions, highlighting the presence of **1-MeCN$^+$** in solution and an authentic sample of **1-MeCN$^+$** for comparison. The 6,6′ peak is highlighted due to its relative insensitivity to changes in ion pairing strength. (**b**) ^{1}H NMR spectra of **2|PF$_6$** in dry MeCN-d_3 showing increasing concentrations of **2-MeCN$^+$** over time.

Scheme 2 Halide substitution equilibrium reactions of **1** and **2** in coordinating solvents.

Table 3 Equilibrium constants and thermodynamic parameters for halide substitution of complexes **1** and **2** under various conditions

	K_{eq}	ΔG_{rxn}/kJ mol^{-1}	ΔH_{rxn}/kJ mol^{-1}	ΔS_{rxn}/J mol^{-1} K^{-1}
1|PF$_6$	$7.94 \pm 0.84 \times 10^{-4}$	17.7 ± 2.7	—	—
"wet"	$1.36 \pm 0.32 \times 10^{-3}$	16.4 ± 0.6	—	—
+TBAPF$_6$ [a]	$5.12 + 0.84 \times 10^{-3}$	13.1 ± 0.4	—	—
+NH$_4$PF$_6$ [a]	$8.50 \pm 0.44 \times 10^{-2}$	5.78 ± 0.20	—	—
1|Cl	2.21 ± 0.10	−2.00 ± 0.12	−4.32 ± 0.26	−8.28 ± 0.88
2|PF$_6$	$4.51 \pm 0.94 \times 10^{-2}$	7.71 ± 0.52	—	—
"wet"	$1.42 \pm 0.05 \times 10^{-1}$	4.83 ± 0.09	—	—
+TBAPF$_6$ [a]	$1.63 \pm 0.05 \times 10^{-1}$	4.50 ± 0.07	—	—
2|Cl	12.4 ± 0.4	−6.23 ± 0.08	—	—
2|Br	14.5 ± 0.6	−6.62 ± 0.10	−10.4 ± 1.0	−12.7 ± 3.3

[a] The concentration of salt in these samples was 100 mM (10 equivalents *vs.* complex).

species grew. The concentration of the new species continued to increase over the course of several days until equilibrium was reached as shown in Fig. 4. The 5,5′ peak of the new species is shifted upfield of the corresponding peak of **2**. All other resonances, including the 6,6′ peak which was insensitive to the identity of the counterion in DMSO, appear downfield of peaks belonging to the parent complex. This behavior is consistent with partial dissociation of the axial Br$^-$ from the complex to generate a mixture of **2** and **2-MeCN$^+$**. The equilibrium constant for the reaction of **2** with MeCN is $K_{eq} = 4.51 \pm 0.94 \times 10^{-2}$, more than two orders of magnitude greater than that of **1|PF$_6$**. Comparison of the equilibrated sample of **2|PF$_6$** to the spectrum of an independently prepared sample of **2-MeCN$^+$** (Fig. S14) supports the assignment of the new species as the product of a halide substitution reaction. The positions of the 6,6′ protons of the pure **2-MeCN$^+$** sample is identical to those of the new species (7.83 ppm), and the 5,5′ protons that appear are shifted by less than 0.01 ppm. The 3,3′ protons in

the pure **2-MeCN$^+$** sample are significantly upfield of both 3,3′ peaks in the equilibrated sample of **2|PF$_6$** due to the absence of free Br$^-$ in solution. The increasing concentration of Br$^-$ in solution results in a downfield shift of the peaks associated with protons in the cationic binding pocket. As the reaction progressed towards equilibrium a large downfield shift in the position of the 3,3′ peaks from both species was observed. The magnitude of the shift was greater for **2-MeCN$^+$** ($\Delta\delta_{\mathbf{2|PF6}}$ = 0.20 ppm, $\Delta\delta_{\mathbf{2\text{-}MeCN+}}$ = 0.34 ppm) implying that more of the liberated Br$^-$ end up associated with the cationic binding pockets of the more highly charged **2-MeCN$^+$** complexes.

For both **1** and **2**, an increase in the equilibrium constant was observed when the spectra were obtained in MeCN-d_3 saturated with atmospheric H_2O ($K_{eq,1}$ = 1.36 ± 0.32 × 10^{-3}, $K_{eq,2}$ = 1.42 ± 0.05 × 10^{-1}) compared to samples prepared using dry solvents in an N_2-filled glovebox. In DMSO-d$_6$, the spectra of the **1|X** and **2|X** complexes are unaffected by the presence of ambient H_2O as shown in Fig. S15 and S16. In wet solvent, the methylene protons of the halide and solvent-bound complexes appear as a singlet rather than the roofed doublet observed in DMSO-d_6, or the weaker splitting observed in dry MeCN-d_3, indicating weaker ion pairing between the tmam^{2+} and PF$_6^-$ ions, possibly due to stronger ion–dipole interactions between the counterion and the H_2O in solution. The observation of increased K_{eq} alongside weaker tmam-halide ion pairing suggests that the dicationic binding pockets are better able to participate in halide dissociation in wet samples. This combined with the faster halide substitution in wet solvent suggests that halide dissociation is rate limiting in the substitution reaction.

The equilibrium between **2** and **2-MeCN$^+$** was observed using UV-vis spectroscopy in anhydrous MeCN over a period of eight hours. The reaction proceeds very slowly, but subtle changes in the UV-vis spectrum were apparent. A spectrum recorded 65 h after sample preparation shows that the substitution continued to progress slowly. The changes over time in the UV-vis spectrum of **2|PF$_6$** map neatly to those observed in the UV-vis spectrum of **2-MeCN$^+$** (Fig. 5). This is shown more clearly in the difference spectrum of **2|PF$_6$** (Fig. 5, inset), which is qualitatively identical to the difference between the initial spectrum of **2|PF$_6$** (t = 1 min) and the spectrum of **2-MeCN$^+$**, further supporting the proposed halide substitution reaction. In agreement with the smaller substitution K_{eq} for **1** in MeCN observed by NMR, the UV-vis spectrum of **1|PF$_6$** in MeCN (Fig. S17) was stable over time and is comparable to the absorption spectrum of **1|PF$_6$** in DMSO.

The ^{1}H NMR spectra of **1** and **2** were collected in MeCN-d_3 with 10 equivalents (100 mM) of TBAPF$_6$ (Fig. 4 and S18, respectively) to examine the effect of excess PF$_6^-$ on K_{eq}. The added TBAPF$_6$ had very little effect on the ^{1}H NMR spectrum of **1**, though a minor upfield shift of the protons in the tmam^{2+} binding pocket was observed, likely due to greater [PF$_6^-$] increasing the occupancy of the tmam^{2+} binding pocket. For **2**, the 3,3′ peak of the parent complex still shifts downfield ($\Delta\delta$ = 0.17 ppm) as the sample reaches equilibrium, but at equilibrium the 3,3′ peak of **2** in the 100 mM TBAPF$_6$ solution

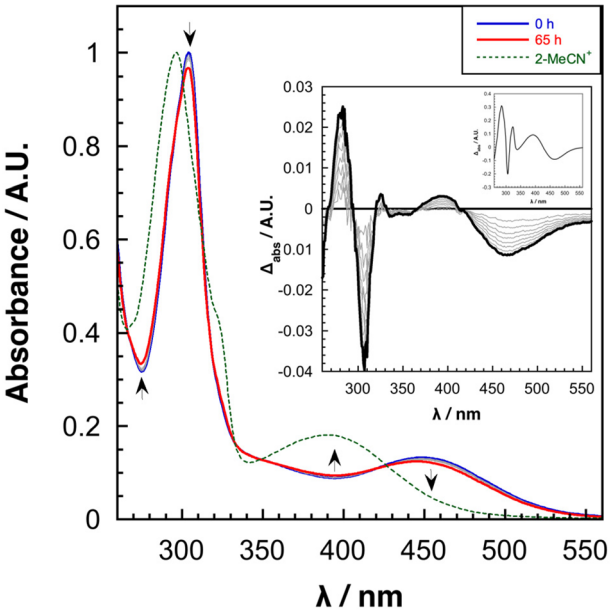

Fig. 5 UV-vis spectra of **2|PF$_6$** in MeCN collected over 65 h as an equilibrium between **2** and **2-MeCN$^+$** is reached. The absorbance spectrum of **2-MeCN$^+$** is included for comparison (dashed). (inset) Difference spectra highlighting the change in the spectra from t = 0 to t = 8 h (black), and the inset spectrum shows the difference between **2|PF$_6$** at t = 0 h and an authentic sample of **2-MeCN$^+$**.

appears slightly upfield (by 0.02 ppm) of the same peak in neat MeCN-d$_3$. This difference is more dramatic for the 3,3′ protons of **2-MeCN$^+$** which shift 0.12 ppm upfield after the addition of TBAPF$_6$. A minor increase in K_{eq} was observed for both **1|PF$_6$** and **2|PF$_6$** compared to samples without TBAPF$_6$ in wet MeCN-d_3 (Table 3). Despite the small K_{eq} measured for the halide substitution reaction of **1|PF$_6$** in MeCN, crystals of **1-MeCN$^+$** were grown from an MeCN solution with excess NH_4PF_6, suggesting that the presence of the electrolyte shifts the equilibrium towards **1-MeCN$^+$**. The ^{1}H NMR spectra of **1|PF$_6$** in MeCN-d_3 with 100 mM NH_4PF_6 initially showed similar concentrations of **1-MeCN$^+$** to samples with TBAPF$_6$. However, after sitting at room temperature in the dark for 12 d, the sample containing NH_4PF_6 displayed significantly higher concentrations of **1-MeCN$^+$**, whereas with TBAPF$_6$ no increase in [**1-MeCN$^+$**] was observed after eighty days, as shown in Fig. 4. Under these conditions, K_{eq} = 9.72 ± 0.80 × 10^{-2} is two orders of magnitude greater than K_{eq} for **1|PF$_6$** in wet MeCN-d_3. Weaker ion pairing was observed in samples containing NH_4PF_6 as an upfield shift of the 3,3′ protons compared to the complex in neat MeCN-d_3 despite much higher [Cl$^-$]. The increase in K_{eq} and the weaker ion pairing can both be attributed to the formation of NH_4Cl (which has limited solubility in MeCN) upon release of Cl$^-$, pushing the substitution equilibrium towards **1-MeCN$^+$**.

To determine the reversibility of the bromide substitution of **2|PF$_6$**, TBABr was added to equilibrated samples of **2|PF$_6$** in MeCN-d_3 with and without TBAPF$_6$. As expected, the addition of TBABr caused the equilibrium between **2** and **2-MeCN$^+$** to

shift back towards **2**. As shown in Fig. S19, addition of one equivalent of TBABr (10 mM) results in a decrease in **2-MeCN$^+$** in both samples, and a second equivalent (20 mM TBABr) almost completely reverses the dissociation reaction. The presence of additional Br^- in solution results in a large downfield shift of the 3,3′ proton resonances due to strong ion pairing between $tmam^{2+}$ and the halide. Notably, the presence of excess $TBAPF_6$ in solution slowed the shift, suggesting competitive binding between PF_6^- and Br^- and the binding pocket. Increasing the concentration of TBABr to 5 eq. in the 100 mM $TBAPF_6$ sample led to the precipitation of **2|Br**. Without excess PF_6^-, **2|Br** began to precipitate with only two equivalents of TBABr.

Halide substitution in H_2O. The halide salts of **1** and **2** are highly soluble in H_2O, allowing for the study of halide substitution under aqueous conditions. In D_2O, the equilibrium for the halide dissociation reaction of **1|Cl** and **2|X** complexes shifts in favor of the solvato species. One recent study of $Re(CO)_3$ complexes bearing ester modified diimine ligands demonstrated similar halide substitution equilibria in aqueous solution.[31] Additionally, this behavior has been reported for an $Mn(CO)_3$ complex bearing a carboxylic acid modified bipyridine. The authors observed the spontaneous formation of the aquo complex ($[Mn(bpy(COOH)_2)(CO)_3(H_2O)]^+$) upon dissolution of the neutral bromide complex in H_2O, and its presence was confirmed using mass spectroscopy, FTIR spectroscopy and UV-vis spectroscopy.[32] The initial NMR spectrum (t = 10 min) is sharp and shows the presence of two distinct $[Re(tmam)(CO)_3L]^{2+}$ species, which are denoted as **1** and **1-H_2O^+**. After one hour, **1-H_2O^+** was the dominant species in solution and its concentration continued to increase until reaching an equilibrium after three hours with K_{eq} = 2.21 ± 0.10 (Fig. S20). The position of the 3,3′ peaks in the D_2O spectrum of **1|Cl** changed very little over the course of the reaction but, as with **2|PF_6** in MeCN-d_3, the downfield shift of the solvato species ($\Delta_{peak,1\text{-}H2O+}$ = 0.12 ppm) is greater than that of the parent complex ($\Delta_{peak,1} \geq$ 0.01 ppm). For **2|X** complexes, the ^{1}H NMR spectra in D_2O show one dominant species in solution as shown in Fig. 6. However, another, much smaller set of tmam peaks upfield from the primary peaks is also visible in the spectrum, indicating that **2** rapidly converts to **2(H_2O)$^+$**. No change in the concentration of the two species was observed over the course of one day. K_{eq} values for **2|Br** and **2|Cl** in D_2O are nearly identical ($K_{eq,\ 2|Cl}$ = 12.4 ± 0.4 and $K_{eq,2|Br}$ = 14.5 ± 0.6). The 3,3′ peaks of all three complexes appear much further upfield in D_2O than in DMSO-d_6, indicating that anion pairing with the $tmam^{2+}$ binding pocket is much weaker in D_2O. This is attributed to a more favorable solvation free energy of the halide in H_2O.[33] No ligand substitution was observed for **1|Cl** or **2|Cl** in CD_3OD (Fig. S21 and S22), despite MeOH and H_2O possessing similar Cl^- and Br^- solvation free energies.[33] This indicates that the stability of the solvato complexes is also key to the thermodynamics of the reaction.

Equilibrated NMR samples of **1|Cl** and **2|Br** were titrated with halide salts to evaluate the reversibility of the halide substitution reaction. KCl was added to a sample of **1|Cl** in D_2O at equilibrium. As expected, the addition of one equivalent of KCl increased the concentration of **1** over the course of 90 minutes as the sample reached an equilibrium. Subsequent

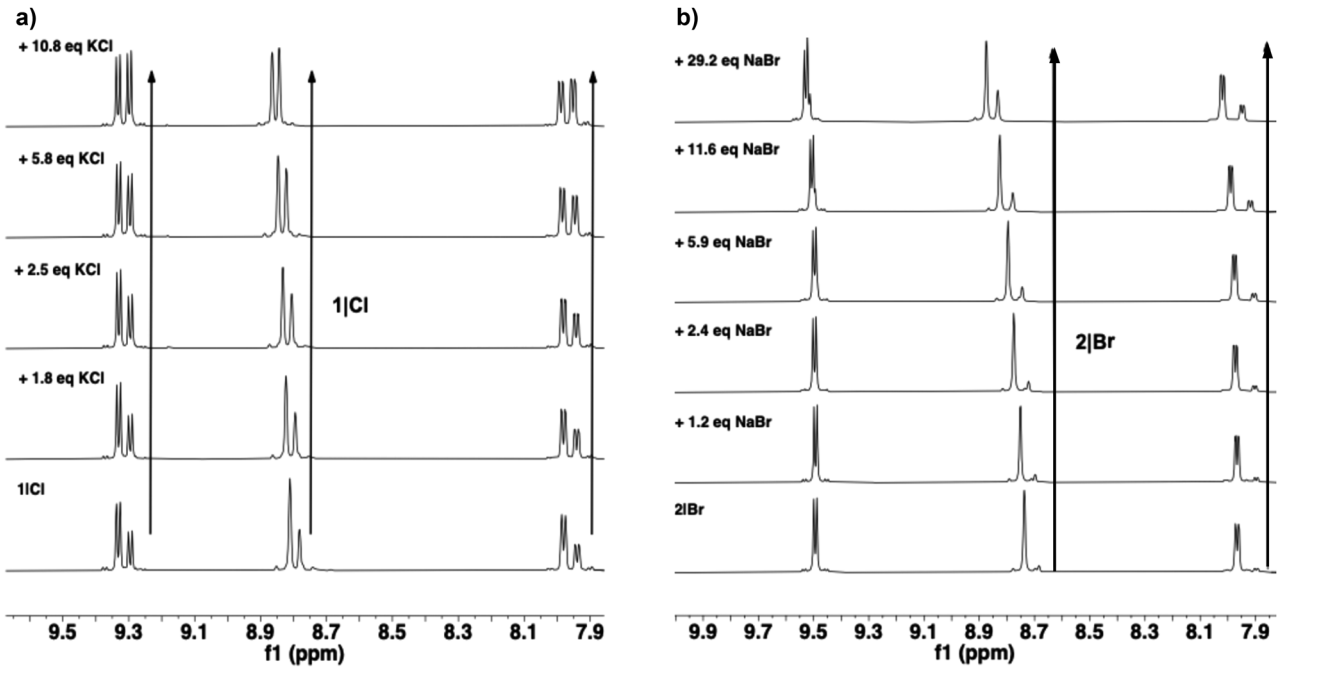

Fig. 6 ^{1}H NMR spectra showing the changes to the $tmam^{2+}$ ligand resonances of (a) **1|Cl** at equilibrium with various amounts of added KCl and (b) **2|Br** at equilibrium with various amounts of added NaBr.

additions of KCl further shifted the equilibrium concentration of **1** as shown in Fig. 6. For **2** the Br^- salt of the complex was used in titration experiments to avoid complications that could arise from the difference in the ion pairing strengths of Cl^- and Br^-. Increasing $[Br^-]$ with additions of NaBr resulted in an increase in the concentration of **2** compared to that of **2-D_2O^+**, but **2-D_2O^+** remained the dominant species in solution up to 20 eq. of Br^- (Fig. 6). For both **1** and **2**, increasing $[X^-]$ in the solution resulted in downfield shifts of the 3,3′, and $N(CH_3)_3$ resonances in the $tmam^{2+}$ binding pockets. The ability to shift the concentration of the equilibrium species confirms that a halide–solvent exchange reaction is in fact the equilibrium being observed. As a control experiment, TBABr was added in aliquots to **2|Br** in DMSO-d_6 (Fig. S23). Outside of the expected downfield shift of the protons in the binding pocket, no other changes were observed with increasing $[Br^-]$.

Variable temperature (VT) ^1H NMR experiments were conducted to determine the enthalpic and entropic contributions to ΔG for the halide displacement reactions. VT experiments for **1|PF_6** and **2|PF_6** were frustrated by the slow interconversion between the parent and solvato complexes in MeCN. For both **1|Cl** and **2|Br**, the concentration of the halide-bound complex increased with increasing temperatures. The spectra and van't Hoff plots for **1|Cl** and **2|Br** are displayed in Fig. S24 and S25, respectively. Halide substitution is slightly exothermic for both complexes and larger for **2** *versus* **1** ($\Delta H_{rxn,1} = -4.32 \pm 0.26$ kJ mol^{-1}; $\Delta H_{rxn,2} = -10.4 \pm 1.0$ kJ mol^{-1}). The more favorable ΔH_{rxn} for **2** can be rationalized by considering the greater hard–soft mismatch between Mn(I) and Br^- than between Re(I) and Cl^-. Both reactions display negative entropy of reaction ($\Delta S_{rxn,1} = -8.28 \pm 0.88$ J mol^{-1} K^{-1}; $\Delta S_{xn,2} = -10.4 \pm 3{,}3$ J mol^{-1} K^{-1}) suggesting an entropic penalty associated with solvation of the tricationic metal complexes and liberated halide, and the greater entropy cost for **2** is consistent with the larger solvation shell needed for the larger Br^- anion.

The halide substitution equilibrium was also observed using UV-vis spectroscopy. Fig. 7 shows the progression of the absorption spectrum following injection of a DMSO stock solution of **1|Cl** into H_2O over the first two hours of the reaction. Isosbestic points are observed at 385 nm, 312, and 287 nm. Over time, the spectra show a blue-shift of the MLCT and peak π–π* absorptions and increasing prominence of the shoulders in $tmam^{2+}$ π–π* transitions. The UV-vis spectrum of **2|Cl** in H_2O (Fig. S26) shows an MLCT absorption at 400 nm, which is consistent with other $[Mn(diimine)(CO)_3(H_2O)]^+$ species in the literature, demonstrating complete conversion of **2** to **2-H_2O^+**.[32,34]

The kinetics of the chloride substitution reaction between **1|Cl** and D_2O was monitored using ^1H NMR. A time series of spectra is shown in Fig. 8a. Typically, under reaction conditions in which $[\mathbf{1}] \ll [D_2O]$, the forward rate should only depend on [**1**], and we expect a first-order dependence on [**1**]. However, the data were better fit by plotting $[\mathbf{1}]^{-1}$ *vs.* *t* (Fig. 8b), indicating that the halide dissociation is second order in [**1**] and the involvement of a second equivalent of **1** in the halide substitution. One potential explanation for this second-order

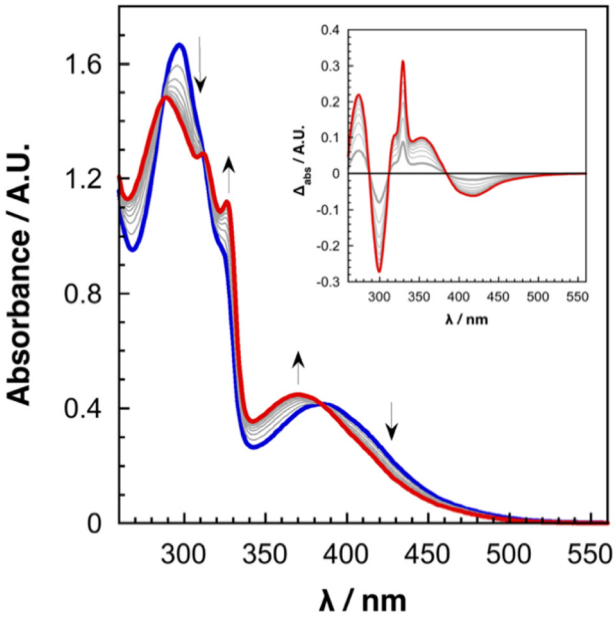

Fig. 7 UV-vis spectra of **1|Cl** in H_2O showing the change in absorbance over 25 min. The arrows indicate the direction of the change in that region. (inset) Difference spectra showing the evolution of the equilibrium between **1|Cl** and **1-H_2O^+**.

dependence is a bimolecular interaction shown in Fig. 8d. Such **1–1** dimers may be supported by favorable π-stacking interactions between the bpy core of the $tmam^{2+}$ ligand and electrostatic interactions between the halides and the $tmam^{2+}$ binding pockets. In this configuration, the pendant ammonium arms of the $tmam^{2+}$ ligand of one complex could stabilize the release of the Cl^- from the other. This hypothesis was based on the observation of a similar interaction between complexes of **1** in a crystal structure of **1|Cl** grown in H_2O with excess NaCl (Fig. 8c). However, disorder in cocrystallized H_2O and NaCl prevented adequate refinement of the data, and this is only circumstantial evidence for the proposed mechanism. Furthermore, the NMR experiments were performed at a single concentration (10 mM), and it is possible that this cooperative reactivity is concentration dependent, and the second order mechanism only dominates at higher concentrations. The observation of halide substitution in UV-vis experiments—in which [**1**] ranged from 0.051 to 0.009 mM—shows that the reaction proceeds at much lower concentrations. Additional experimental work is required to provide a more complete analysis of this substitution mechanism. At this point, we cannot rule out alternative halide substitution mechanisms.

Electrochemical characterization

Non-aqueous electrochemistry. Group 7 tricarbonyl complexes are well-known CO_2 reduction electrocatalysts.[1–9,13–17,35] However, previous studies have shown that the $tmam^{2+}$ ligand is reductively unstable.[18,20] More specifically, a recent report on a close analogue of **1|PF_6**—differing only in the identity of the axial halide (Cl *vs.* Br)—provides evidence that the $tmam^{2+}$

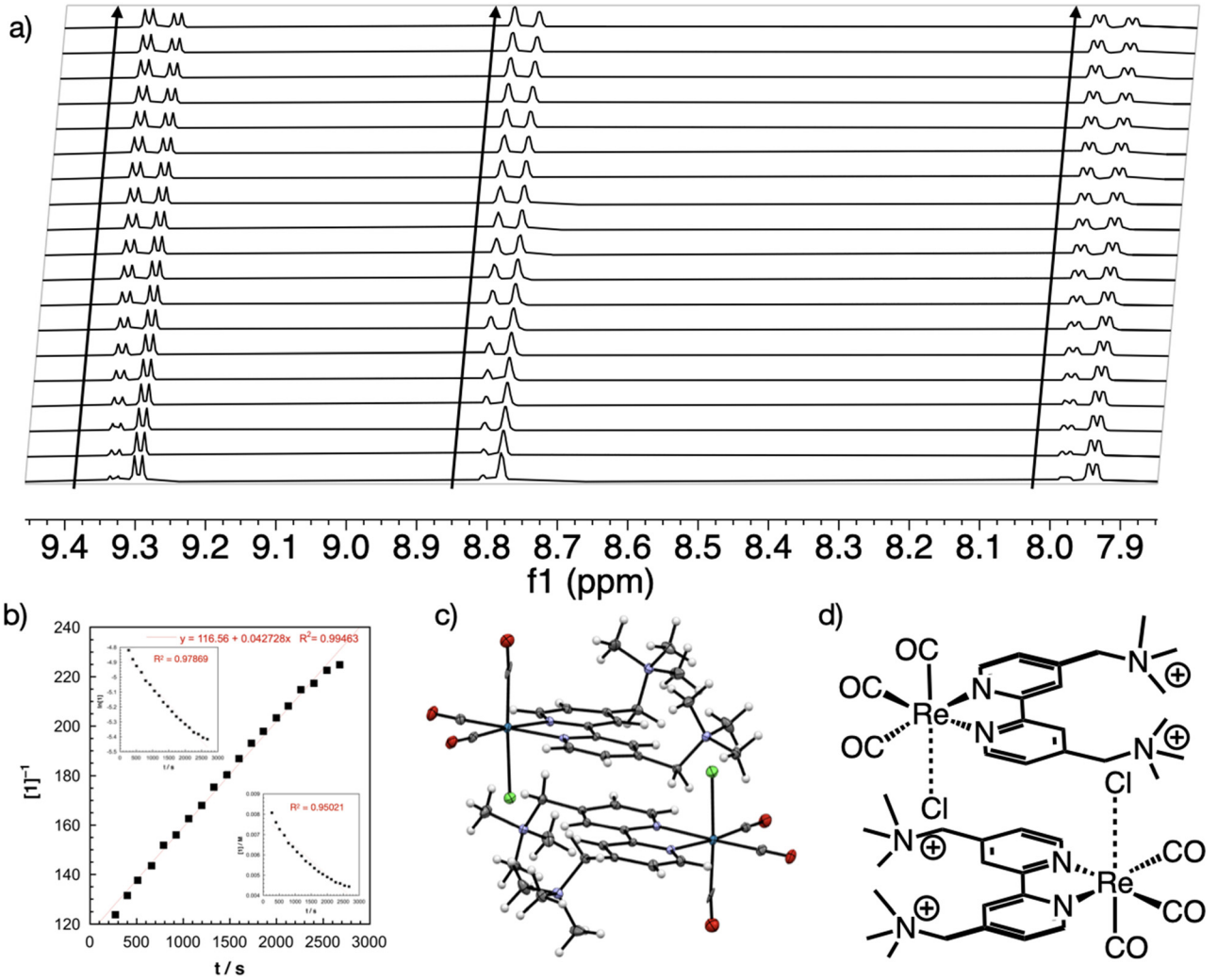

Fig. 8 (a) ^{1}H NMR spectrum of **1|Cl** (10 mM) in D_2O showing the evolution of the equilibrium between **1** and **1(H$_2$O)$^+$**. (b) Linear second-order fit of the kinetics data from (a) (inset top) and non-linear first-order fit (inset bottom) plot of concentration *vs.* time of **1** from the NMR data in (a). (c) Disordered crystal structure that supports the observed second-order dependence of **1** on the rate of chloride substitution. (d) Proposed **1–1** intermolecular interactions that could support halide dissociation.

ligand undergoes reductive deamination, releasing NMe_3 and generating a methylene radical, which is proposed to ultimately form Re(dmb)(CO)$_3$Br (dmb = 4,4′-dimethyl-2.2′-bipyridine).[18] Considering this, the electrocatalytic properties of these complexes will not be discussed. For all peaks in the CVs of **1** and **2**, plots of peak height *vs.* $\nu^{1/2}$ (50–1600 mV s^{-1}) are linear for the initial voltage sweep consistent with the complexes being freely diffusing species (Fig. S27 and S28). However, evidence for deposition was observed for **1|PF$_6$** in MeCN when the CVs were repeated for multiple cycles (Fig. S29) and, care was taken to polish the glassy carbon (GC) working electrode surface between each scan to ensure that the measurements reflect the behavior of the bulk solution. Cyclic voltammograms (CVs) of **1|PF$_6$**, **1-MeCN$^+$**, **2|PF$_6$** and **2-MeCN$^+$** were obtained in N_2-purged MeCN with 0.1 M $TBAPF_6$ as the supporting electrolyte and are shown in Fig. 9, and all potentials for non-aqueous experiments are reported *versus* a ferrocene/ferrocenium internal standard (V *vs.* Fc$^{+/0}$). Neither the solvent nor the electrolyte was rigorously dried prior to these measurements.

The CV profile of **1|PF$_6$** (Fig. 9a) shows a broad irreversible reduction with E_{pc} = −1.38 V and a second partially reversible reduction with $E_{1/2}$ = −1.86 V. The use of the term "partially reversible" here indicates the observation of some return current on the reverse scan, but the redox couple is not strictly electrochemically reversible. Two, smaller reductions appear at more negative potentials; the first of these is irreversible (E_{pc} = −2.05), and the second is partially reversible ($E_{1/2}$ = −2.26 V). Return scans show a small anodic peak (E_{pc} = −0.50 V) corresponding to the Re^0–Re^0 dimer.[18,36] The reduction at −1.38 V has been previously assigned to be a 1-electron reduction of the tmam^{2+} ligand and results in ligand degradation. However, there is a cathodic shoulder of the main peak at −1.45 V which is visible at 100 mV s^{-1} and the peak height of the combined

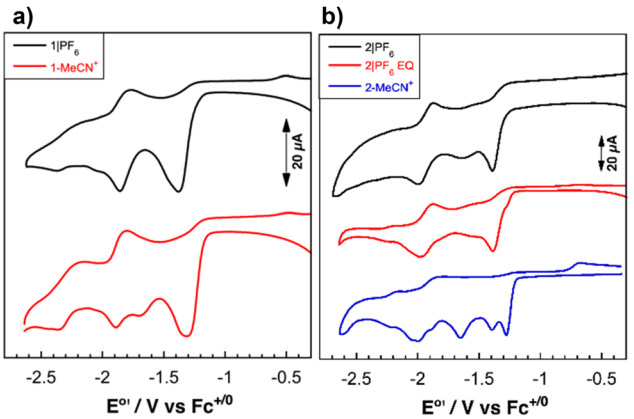

Fig. 9 (a) Cyclic voltammograms of **1|PF$_6$** (black) and **1-MeCN$^+$** (red). (b) Cyclic voltammograms of a freshly prepared solution of **2|PF$_6$** (black), a solution of **2|PF$_6$** that had been in solution for 1 d (red), and **2-MeCN$^+$** (blue). All data were collected at a scan rate of 100 mV s^{-1} in N_2-purged MeCN with 0.1 M $TBAPF_6$ supporting electrolyte with 1 mM complex.

feature is ~2 times that of the subsequent peak at all scan rates (50–1600 mV s^{-1}). At scan rates > 400 mV s^{-1}, the shoulder becomes the dominant peak, providing additional support for the assignment of the peak as two overlapping reductions. This behavior likely arises from sequential EC processes in which reduction (electrochemical step, E) localized on the tmam^{2+} ligand leads to reductive deamination of the tmam^{2+} ligand (chemical step C) to generate a monocationic ligand that can undergo a second EC process (generating a second equivalent of NMe_3) at more negative potentials due to the reduced positive charge on the ligand. At low scan rates ($\nu \leq 200$ mV s^{-1}), the voltammograms show little change when the voltage range is swept a second time, but when $\nu \geq 400$ mV s^{-1}, the magnitude of the first reduction feature is significantly smaller in the second cycle (Fig. S30). Peak heights for the other features do not change with multiple scans. This is consistent with the assignment of the first cathodic feature as a ligand degradation process. At faster scan rates, the deaminated complexes produced in the first sweep do not have time to fully diffuse away from the electrode surface, and there is a lower concentration of **1** in the diffusion layer leading to decreased current for the reduction associated with the reductive deamination.

In CVs of Re(bpy)(CO)$_3$Cl, substitution of the axial Cl$^-$ for MeCN produces a large positive shift in the Re-centered reduction, from −2.14 to −1.78 V, but the ligand-centered reduction is less sensitive to axial ligand substitution.[36–38] For **1-MeCN$^+$** (Fig. 9a), a small positive shift of the tmam-centered reductions is observed (E_{pc} = −1.36 V). A new irreversible reduction with E_{pc} = −1.69 V *vs.* Fc$^{+/0}$ appears between the tmam^{2+} reductions, which may be a Re$^{I/0}$ feature. A reduction at −1.84 V appears at very similar potentials to the corresponding reduction of **1**. The peak at −2.23 V is consistent between CVs of **1** and **1-MeCN$^+$**, but the reduction at −2.05 V is no longer observed for **1-MeCN$^+$**. The conservation of the reduction at −1.84 V indicates that this is not a Re centered reduction. Instead, it is likely a reduction of the neutral, deaminated bipyridine ligand, and its reduction potential is very close to the ligand centered reduction of Re(dmb)(CO)$_3$Cl ($E_{1/2}$ = −1.89 V).[5,38] This assignment agrees with the ligand degradation pathway proposed by Thoi *et al.* However, unambiguous assignment of the catalytically relevant redox events of **1** is made difficult by those reductions occurring at potentials cathodic of the reductive degradation of the ligand. Additionally, because the reductive deamination of the tmam^{2+} ligand may be accompanied by halide dissociation, we are unable to make claims regarding the effect of the ligand substitution equilibrium on the electrochemical behavior of these complexes, unless the identity of the axial ligand results in notable differences in the deamination events.

The CVs of **2|PF$_6$** are shown in Fig. 9b. Cathodic scans reveal an irreversible, 2-electron reduction with E_{pc} = −1.40 V, which is attributed to the tmam^{2+} reductive deamination. In this case, there is no apparent potential difference between the first and second EC steps. As with **1|PF$_6$**, a decrease in peak current is observed in subsequent scans following the first voltage sweep (Fig. S31). At more negative potentials, there is a broad, irreversible, cathodic feature (E_{pc} = −1.66) and a partially reversible 1-electron reduction ($E_{1/2}$ = −1.92 V). In the return scan, the dimer oxidation is observed at −0.69 V. Previous studies have established the reductive electrochemistry of Mn(dmb)(CO)$_3$Br (dmb = 4,4′-dimethyl-2,2′-bipyridine). The complexes undergo an irreversible, 1-e$^-$, L(π*)-localized reduction at E_{pc} = −1.73 V, which induces rapid dissociation of that axial bromide, producing a Mn^0(dmb)(CO)$_3$ metalloradical species that then forms a Mn^0–Mn^0 dimer. Subsequently, the dimer is reduced in an irreversible, 2-e$^-$ process (E_{pc} = −1.90 V), fragmenting the dimer into two [Mn(dmb)(CO)$_3$]$^-$ species.[39] The reported electrochemical behavior of [Mn(dmb)(CO)$_3$(MeCN)]$^+$ is nearly identical to its neutral analogue, (Mn(dmb)(CO)$_3$Br).[39] The first reduction is shifted 140 mV more positive, but the potential of the dimer reduction is unchanged. Similarly, voltammograms in Fig. 9b show that the electrochemical behavior of **2-MeCN$^+$** is, broadly, like that of **2**. The CVs of **2-MeCN$^+$** (Fig. 9b) show two irreversible reductions near the potential at which the first tmam^{2+} reductions were observed for **2**. Interestingly, in the reductive deamination, events are split in the solvato complex. The first reduction is shifted more positive than the 2-electron feature of **2** (E_{pc} = −1.27 V), and the second reduction is at nearly the same potential as the corresponding reduction of **2** (E_{pc} = −1.38 V). The irreversible reduction at −1.65 V *vs.* Fc$^{+/0}$ is still present in the CVs of **2-MeCN$^+$**. A complicated mixture of overlapping reductions between −1.88 V and −2.05 V *vs.* Fc$^{+/0}$ is observed at similar potentials to the Mn-centered, third reduction of **2**. The splitting of this reduction into several new signals with similar potentials implies the presence of multiple Mn species in the diffusion layer.

The changes in the 2-electron reductive deamination of tmam^{2+} between the **2** and **2-MeCN$^+$** complexes allowed for the observation of the halide substitution equilibrium on the electrochemical behavior of **2**. The CVs of samples of **2** that

were stored in electrolyte solution in the dark for 2 days prior to data collection were obtained and compared to those CVs taken immediately after sample preparation. Qualitatively, the CVs of the two samples are very similar; however, CVs of the equilibrated sample (Fig. 9b) show a small anodic shoulder at the foot of the 2-electron $tmam^{2+}$ reduction (−1.27 V), which reveals the presence of **2-MeCN$^+$**. Indeed, this feature is often observed in samples of **2|PF$_6$** within one hour of solution preparation. In agreement with observations *via* ^{1}H NMR and IR, this shoulder was not observed in samples that were allowed to reach an equilibrium in the presence of two equivalents of TBABr (Fig. S32). As noted above, further analysis of the effects of the ligand exchange on the electrochemistry of **2** is prevented by the irreversibility of the ligand degradation process.

Aqueous electrochemistry. Due to their low solubility in H_2O, the aqueous electrochemical properties of M(diimine)$(CO)_3$X (M = Re, Mn) complexes have primarily been studied heterogeneously, with complexes immobilized on an electrode surface.[40–43] A few examples of homogeneous, aqueous electrochemical characterization of these complexes have been reported.[32,44,45] The high solubility of the halide salts of **1** and **2** in H_2O allows for the collection of homogeneous, aqueous CV data for these complexes. The CV of **1|Cl** (1 mM) in N_2 purged 0.1 M $NaClO_4$ electrolyte solution is shown in Fig. 10. All potentials for aqueous electrochemistry are reported *versus* a saturated calomel reference electrode (V *vs.* SCE). Complex **1** displays two reductions within the solvent window. The first reduction is a broad peak with E_{pc} = −1.16 V and is attributed to a reduction of the $tmam^{2+}$ ligand. A second reduction (E_{pc} = −1.41 V) is also observed. If the voltage was scanned past −1.50 V, a large increase in current (likely hydrogen evolution) was observed. Interestingly, no dimer oxidation was detected, but on the return anodic scan an oxidation was observed at E_{pa} = −1.01 V. It is possible that this oxidation is related to the absence of a dimer signal, and the substitution of the halide ligand in a chemical step before the reduction may contribute to this behavior. The first reduction of **1** is likely the same ECEC reductive deamination process observed in MeCN.

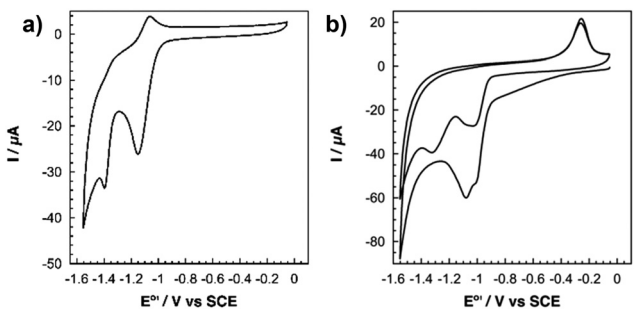

Fig. 10 (a) Cyclic voltammogram of a freshly prepared solution of **1|Cl**. (b) Cyclic voltammogram of a freshly prepared solution of **2|Br**, the feature at −1.28 V *vs.* SCE appears in the second cycle. All data shown were collected at a scan rate of 100 mV s^{-1} in an N_2-purged aqueous 0.1 M $NaClO_4$ electrolyte solution with 1 mM complex.

When the potential range was scanned a second time, the height of the first reduction decreased significantly (E_{pc} does not change), and a slight shoulder appears at potentials more positive of E_{pc}; the second reduction was unaffected by repeated cycling (Fig. S33). To assess the effect of the halide substitution equilibrium on the electrochemical behavior of **1** in H_2O, CVs were obtained for a sample that was allowed to equilibrate in the dark for a period of 1 day. Only minor changes were observed in the CVs of the equilibrated sample (Fig. S34). There was no shift in the potential of the first reduction. Voltammograms of **1** were also collected in 0.1 M $NaClO_4$ with 5 mM and 20 mM added KCl, and in 0.1 M NaCl electrolyte (Fig. S35). Despite the observation of the shifting equilibrium by NMR, CVs of these complexes in the presence of added halide show no change compared to the sample in 0.1 M $NaClO_4$. Although spectroscopic evidence suggests there should be a sizable concentration of **1-H$_2$O$^+$** in the solution shortly after the sample is dissolved in water, the presence of multiple species is not readily apparent in the electrochemical data. This indicates that the aqueous electrochemical behavior of **1** is largely independent of the identity of the axial ligand in H_2O.

The CV **2|Cl** in N_2 purged pH 4.75, 0.1 M $NaClO_4$ (Fig. 10b) shows two overlapping, irreversible reductions at −1.01 V and −1.08 V. These peaks appear similar to peaks assigned to $tmam^{2+}$ reductions for **1|PF$_6$** in MeCN. At a scan rate of 100 mV s^{-1}, no other reductions are visible on the first scan, but scans at 50 mV s^{-1} (Fig. S36) reveal an additional broad reduction at −1.22 V; this is likely a metal centered reduction. Unlike with **1**, aqueous CVs of **2** show a clear dimer oxidation peak at −0.26 V. Significant changes in the voltammogram are observed on a second scan of the voltage range (Fig. 10b). In accordance with observations for **1**, the $tmam^{2+}$ reductions show diminished peak height after the first cycle, which is consistent with ligand degradation. Additionally, the Mn centered reduction becomes significantly more prominent and is shifted, cathodically, to −1.28 V in the second cycle. This behavior may arise from the conversion of multiple Mn species—which would result in multiple smaller peaks that could be lost in the baseline current—to a single, more well-defined species. This would also explain the observation of the more well-defined Mn-centered reduction at slower scan rates. CVs of **2** were also collected in 0.1 M $NaClO_4$ with 5 mM and 20 mM of added NaBr. As with **1**, the addition of NaBr had little effect on the CVs of **2** in aqueous solution (Fig. S37).

Conclusions

Complexes **1|X** and **2|X** have allowed us to investigate the effect of proximal positively charged groups and their counterions on the electronic, structural, and electrochemical characteristics of Re and Mn tricarbonyl complexes. Using the ^{1}H NMR shifts of bipyridine protons as a measurement of anion binding strength with the cationic binding pockets of $tmam^{2+}$, we observe that the size of the ion is a major factor in binding

strength. The identity of the anion has little effect on the electronic structure of the complexes as evidenced by the lack of changes in the UV-vis spectra of the complexes. However, the cationic pendant groups of $tmam^{2+}$ facilitate spontaneous exchange of the axial halide for solvent molecules in an equilibrium process. Equilibrium constants determined using ^1H NMR spectroscopy show that the favorability of the exchange depends on the metal and the solvent. Halide exchange was only observed in MeCN and H_2O, but not in DMSO or MeOH. Weaker anion-tmam ion-pairing in MeCN than in DMSO was observed in ^1H NMR, and anion binding was still weaker in D_2O. This is the inverse of the trend in halide lability for these complexes. The lower ion-pairing strength is also indicative of the stability of the solvated anion. Solvents that can better support the free anion pull the counterion away from the $tmam^{2+}$, which may then drive the substitution in part to stabilize the empty cationic binding pockets.

The strength of the M–X bond is also a key factor in halide substitution. Thermodynamic parameters obtained from VT-NMR studies of **1|Cl** and **2|Br** in H_2O demonstrate that halide substitution is more enthalpically favored for **2** than **1**. The greater hard–soft mismatch in Mn–Br likely contributes to the more favorable halide dissociation observed for Mn than Re. Additional studies using a series of Re–X complexes (X = Cl, Br, I) would be required to better understand this aspect of chemistry. Time course ^1H NMR data for **1** in D_2O suggest that the ligand substitution is second-order in **1**, which suggests an intermolecular process in which halide dissociation from one complex is stabilized by the dicationic binding pocket of a separate complex. Our hypothesis is based on the observation of this interaction in low-quality X-ray crystal structures of **1**. A more detailed study would be required to confirm this hypothesis.

The observed halide substitution reaction had little effect on the observed electrochemical response of complexes **1** and **2** in both MeCN and H_2O. This is due to the reductive instability of the $tmam^{2+}$ ligand, which is observed to undergo reductive deamination at potentials anodic of the ligand- and metal-centered reductions of the catalyst. If halide dissociation occurs alongside the reductive deamination (producing a solvato complex), one would expect the potential of subsequent reductions to have little dependence on the identity of the axial ligand in the bulk sample. An alternative ligand framework is required to study the potential effects of pendant group-assisted ligand substitution on the electrochemical and electrocatalytic behavior of these catalysts.

The installation of pendant functional groups that can participate in catalytic reactions through the secondary coordination sphere has been fruitful in improving the performance of molecular electrocatalysts for a variety of reactions. This study shows that these functional groups can produce unexpected reactivity. Our examination into the effects of the cationic pendant groups of the $tmam^{2+}$ ligand on the coordination chemistry of Re and Mn $M(DI)(CO)_3X$ complexes has shown that these groups are noninnocent in their interactions with the X-type halide ligand. Understanding these interactions can suggest how these functional groups support catalytic reactions by participating in catalyst activation and their ability to stabilize charged catalytic intermediates.

Author contributions

WK, BS, and TS contributed to the conceptualization and supervision of this work. They also contributed to the methodology employed in this work. WK, BS, TS, and JPV contributed as investigators and validators for the synthesis and spectroscopic characterization of compounds reported herein. WK, TS, JPV, CB, AB, and CL contributed as investigators for the electrochemical experiments. WK wrote the original draft of this manuscript. WK, BS and TS contributed to reviewing and editing the written manuscript.

Conflicts of interest

There are no conflicts to declare.

Data availability

Supplementary information (SI): experimental details, spectroscopic data used for characterization of complexes (UV-vis, FTIR, ^1H NMR), ^1H NMR data demonstrating halide substitution for all complexes as detailed in the text, and additional electrochemical characterization for all complexes. See DOI: https://doi.org/10.1039/d5dt02433a.

All experimental data are available upon request from the corresponding author: (wkramer@hamilton.edu).

CCDC 2494313–2494315 contain the supplementary crystallographic data for this paper.[46a–c]

Acknowledgements

This project was conceived and initial work was performed in the lab of Prof. Harry B. Gray and funded by NSF CCI Solar Fuels (CHE-130124). Additional support was provided at Caltech and a Dr and Mrs Daniel C. Harris SURF Fellowship. The authors acknowledge Harry B. Gray for his unwavering support and exceptional mentorship. The authors also acknowledge Brendon J. McNicholas for his helpful contributions during the writing of this manuscript, and we thank Larry Henling and Michael Takase for their assistance with X-ray crystallography experiments.

References

1 J. Hawecker, J. M. Lehn and R. Ziessel, *Helv. Chim. Acta*, 1986, **69**, 1990–2012.
2 J. Hawecker, J.-M. Lehn and R. Ziessel, *J. Chem. Soc., Chem. Commun.*, 1984, 328–330.

3 J. M. Smieja, M. D. Sampson, K. A. Grice, E. E. Benson, J. D. Froehlich and C. P. Kubiak, *Inorg. Chem.*, 2013, **52**, 2484–2491.
4 L. Rotundo, E. Azzi, A. Deagostino, C. Garino, L. Nencini, E. Priola, P. Quagliotto, R. Rocca, R. Gobetto and C. Nervi, *Front. Chem.*, 2019, **7**, 417.
5 M. L. Clark, P. L. Cheung, M. Lessio, E. A. Carter and C. P. Kubiak, *ACS Catal.*, 2018, **8**, 2021–2029.
6 G. F. Manbeck, J. T. Muckerman, D. J. Szalda, Y. Himeda and E. Fujita, *J. Phys. Chem. B*, 2015, **119**, 7457–7466.
7 M. D. Sampson, A. D. Nguyen, K. A. Grice, C. E. Moore, A. L. Rheingold and C. P. Kubiak, *J. Am. Chem. Soc.*, 2014, **136**, 5460–5471.
8 F. Franco, C. Cometto, L. Nencini, C. Barolo, F. Sordello, C. Minero, J. Fiedler, M. Robert, R. Gobetto and C. Nervi, *Chem. – Eur. J.*, 2017, **23**, 4782–4793.
9 F. Franco, C. Cometto, F. F. Vallana, F. Sordello, E. Priola, C. Minero, C. Nervi and R. Gobetto, *Chem. Commun.*, 2014, **50**, 14670–14673.
10 L. Rotundo, C. Garino, E. Priola, D. Sassone, H. Rao, B. Ma, M. Robert, J. Fiedler, R. Gobetto and C. Nervi, *Organometallics*, 2018, **38**, 1351–1360.
11 I. Siewert, *Acc. Chem. Res.*, 2022, **55**, 473–483.
12 I. Azcarate, C. Costentin, M. Robert and J.-M. Savéant, *J. Am. Chem. Soc.*, 2016, **138**, 16639–16644.
13 L. Rotundo, S. Ahmad, C. Cappuccino, D. E. Polyansky, M. Z. Ertem and G. F. Manbeck, *Inorg. Chem.*, 2023, **62**, 7877–7889.
14 L. Rotundo, S. Ahmad, C. Cappuccino, A. J. Pearce, H. Nedzbala, S. R. Bottum, J. M. Mayer, J. F. Cahoon, D. C. Grills, M. Z. Ertem and G. F. Manbeck, *J. Am. Chem. Soc.*, 2024, **146**, 24742–24747.
15 S. Sung, X. Li, L. M. Wolf, J. R. Meeder, N. S. Bhuvanesh, K. A. Grice, J. A. Panetier and M. Nippe, *J. Am. Chem. Soc.*, 2019, **141**, 6569–6582.
16 S. Sung, D. Kumar, M. Gil-Sepulcre and M. Nippe, *J. Am. Chem. Soc.*, 2017, **139**, 13993–13996.
17 N. R. Crudo, A. Sonea, L. M. Karn, D. B. Leznoff and J. J. Warren, *ACS Catal.*, 2025, **15**, 14293–14304.
18 S. S. Saund, M. A. Siegler and V. S. Thoi, *Inorg. Chem.*, 2021, **60**, 13011–13020.
19 L. Troian-Gautier, S. A. M. Wehlin and G. J. Meyer, *Inorg. Chem.*, 2018, **57**, 12232–12244.
20 W. B. Swords, G. Li and G. J. Meyer, *Inorg. Chem.*, 2015, **54**, 4512–4519.
21 S. A. M. Wehlin, L. Troian-Gautier, R. N. Sampaio, L. Marcélis and G. J. Meyer, *J. Am. Chem. Soc.*, 2018, **140**, 7799–7802.
22 S. A. M. Wehlin, L. Troian-Gautier, G. Li and G. J. Meyer, *J. Am. Chem. Soc.*, 2017, **139**, 12903–12906.
23 L. Troian-Gautier, W. B. Swords and G. J. Meyer, *Acc. Chem. Res.*, 2018, **52**, 170–179.
24 A. M. Deetz, M. J. Goodwin, E. A. Kober and G. J. Meyer, *Inorg. Chem.*, 2023, **62**, 11414–11425.
25 L. Troian-Gautier, E. E. Beauvilliers, W. B. Swords and G. J. Meyer, *J. Am. Chem. Soc.*, 2016, **138**, 16815–16826.
26 J. V. Caspar and T. J. Meyer, *J. Phys. Chem.*, 1983, **87**, 952–957.
27 J. M. Smieja and C. P. Kubiak, *Inorg. Chem.*, 2010, **49**, 9283–9289.
28 M. D. Sampson and C. P. Kubiak, *J. Am. Chem. Soc.*, 2016, **138**, 1386–1393.
29 M. Jakonen, L. Oresmaa and M. Haukka, *Cryst. Growth Des.*, 2007, **7**, 2620–2626.
30 M. A. Bento, N. A. G. Bandeira, H. N. Miras, A. J. Moro, J. C. Lima, S. Realista, M. Gleeson, E. J. Devid, P. Brandão, J. Rocha and P. N. Martinho, *Inorg. Chem.*, 2024, **63**, 18211–18222.
31 T. Pivarcsik, J. Kljun, S. C. Rodriguez, D. C. Alcaraz, U. Rapuš, M. Nové, E. F. Várkonyi, J. Nyári, A. Bogdanov, G. Spengler, I. Turel and E. A. Enyedy, *ACS Omega*, 2024, **9**, 44601–44615.
32 J. J. Walsh, G. Neri, C. L. Smith and A. J. Cowan, *Organometallics*, 2019, **38**, 1224–1229.
33 C. P. Kelly, C. J. Cramer and D. G. Truhlar, *J. Phys. Chem. B*, 2007, **111**, 408–422.
34 T. N. Twala, M. Schutte-Smith, A. Roodt and H. G. Visser, *Dalton Trans.*, 2015, **44**, 3278–3288.
35 D. C. Grills, M. Z. Ertem, M. McKinnon, K. T. Ngo and J. Rochford, *Coord. Chem. Rev.*, 2018, **374**, 173–217.
36 B. P. Sullivan, C. M. Bolinger, D. Conrad, W. J. Vining and T. J. Meyer, *J. Chem. Soc., Chem. Commun.*, 1985, 1414–1416.
37 M. McKinnon, K. T. Ngo, S. Sobottka, B. Sarkar, M. Z. Ertem, D. C. Grills and J. Rochford, *Organometallics*, 2018, **38**, 1317–1329.
38 A. I. Breikss and H. D. Abruña, *J. Electroanal. Chem. Interfacial Electrochem.*, 1986, **201**, 347–358.
39 M. Bourrez, F. Molton, S. Chardon-Noblat and A. Deronzier, *Angew. Chem., Int. Ed.*, 2011, **50**, 9903–9906.
40 S. Sinha, A. Sonea, W. Shen, S. S. Hanson and J. J. Warren, *Inorg. Chem.*, 2019, **58**, 10454–10461.
41 S. Sinha, A. Sonea, C. A. Gibbs and J. J. Warren, *Dalton Trans.*, 2020, **49**, 7078–7083.
42 E. Gala, G. C. D. Bandomo, M. Vettori, S. Royuela, M. Martínez-Fernández, J. I. Martínez, E. Salagre, E. G. Michel, F. Zamora, J. Lloret-Fillol and J. L. Segura, *J. Mater. Chem. A*, 2025, **13**, 1142–1152.
43 A. Zhanaidarova, S. C. Jones, E. Despagnet-Ayoub, B. R. Pimentel and C. P. Kubiak, *J. Am. Chem. Soc.*, 2019, **141**, 17270–17277.
44 C. Das, S. Ghosh, R. Biswas, G. K. Lahiri and A. Dutta, *Chem. Commun.*, 2024, **60**, 10492–10495.
45 A. Nakada and O. Ishitani, *ACS Catal.*, 2017, 354–363.
46 (*a*) CCDC 2494313: Experimental Crystal Structure Determination, 2026, DOI: 10.5517/ccdc.csd.cc2pqjqp; (*b*) CCDC 2494314: Experimental Crystal Structure Determination, 2026, DOI: 10.5517/ccdc.csd.cc2pqjrq; (*c*) CCDC 2494315: Experimental Crystal Structure Determination, 2026, DOI: 10.5517/ccdc.csd.cc2pqjsr.